AAS 19-096

GPS BASED AUTONOMOUS NAVIGATION STUDY FOR THE LUNAR GATEWAY

Luke B. Winternitz, *NASA Goddard Space Flight Center*,
William A. Bamford, *Emergent Space Technologies, Inc.*,
Anne C. Long, *a.i. solutions*,
Munther Hassouneh, *NASA Goddard Space Flight Center*

This paper describes and predicts the performance of a conceptual autonomous GPS-based navigation system for NASA's planned Lunar Gateway. The system is based on the flight-proven Magnetospheric Multiscale (MMS) GPS navigation system augmented with an Earth-pointed high-gain antenna and, optionally, an atomic clock. High-fidelity simulations, calibrated against MMS flight data and making use of GPS transmitter patterns from the GPS Antenna Characterization Experiment project, are developed to predict performance of the system in the Gateway Near-Rectilinear Halo Orbit. The results indicate that GPS can provide an autonomous, realtime navigation capability with comparable, or superior, performance to a ground-based Deep Space Network approach using eight hours of tracking data per day.

INTRODUCTION

NASA has developed an ambitious plan to return to the Moon within the next few years. It begins with the Orion spacecraft's first planned lunar flight in 2020. This will be followed by the first component of a space station known as the Lunar Orbital Platform-Gateway or simply *Gateway* in 2022. Two years later the habitation modules will arrive enabling an extended human presence around the Moon [7]. This lunar push is expected to be mirrored by other space agencies and commercial entities. One challenge common to all of these efforts will be the generation of accurate, real-time, potentially onboard, navigation solutions. Traditionally, lunar missions have relied on ground tracking using the Deep Space Network (DSN) as their baseline approach for navigation. However, the cost, performance, and availability limitations of DSN, especially with a proliferation of commercial lunar spacecraft, could be problematic for many missions. Furthermore, the demonstrated cost and science benefits of onboard navigation would not be realized through ground based navigation algorithms. In the case of Gateway, autonomous navigation could be especially beneficial during extended periods of uncrewed operations. The system could also function as a key navigation and timing infrastructure component for other payloads and experiments on the Gateway. In this paper, we show that Global Positioning System (GPS) and Global Navigation Satellite System (GNSS)-based navigation can provide a practical, low-cost, high-performance autonomous navigation solution for Gateway and other missions in the lunar regime.*

Over the past two decades, NASA and its partners have extended the applicability for GPS-based space navigation to users beyond Low-Earth Orbit (LEO). On the constellation side, we are working to expand the high-altitude Space Service Volume (SSV) of GPS and multi-GNSS systems [2]. We are also developing and refining high-altitude GPS receiver technology to push the envelope of potential applications [13, 12]. This effort has culminated in a significant breakthrough that has occurred over the last few years, as several civilian missions have demonstrated the benefits of onboard, high-altitude GPS-based navigation. Some

*While this paper focuses primarily on GPS-based navigation, its conclusions generally apply to GNSS-based navigation as well.

notable missions include the Geostationary Operational Environmental Satellite (GOES)-16 and 17 missions, launched November 2016 and March 2018, respectively, operating at Geosynchronous Earth Orbit (GEO). More relevant to the present work is the record-setting Magnetospheric Multiscale (MMS) mission (launched March 2015) that has demonstrated excellent onboard GPS-based navigation in a highly elliptic orbit with a current apogee radius of 25 RE (40% of the lunar distance) and planned apogee of 29 RE. These advances have paved the way towards the next frontier for the high-altitude GPS/GNSS, the cis-lunar and lunar regimes, which we explore in this paper for NASA's Lunar Gateway.

The remainder of the paper is organized as follows. First, we analyze a simplified GPS problem to illustrate a challenge of high-altitude GPS navigation, viz., that range and clock errors tend to dominate the lateral errors. We also discuss a few mitigations. Next, we review the MMS GPS-based navigation system and describe how it can be adapted for the Gateway application through the addition of a high-gain antenna and an optional atomic clock. The subsequent section describes the high-fidelity simulation that we employed for this study, where we focus on the careful calibration of the simulated GPS sidelobe signal levels using MMS flight data. Next, we describe the configuration of our simulation to model both *uncrewed* and *crewed* Gateway scenarios, patterned after the setup in [11]. We also discuss the development of our baseline Ground Station (GS) tracking scenario. Finally, we compare results from Monte Carlo simulations of three different navigation schemes run for a crewed and uncrewed Gateway: a GS tracking baseline, GPS with an MMS-like Ultra-Stable Oscillator (USO), and GPS with a commercial space-rated atomic clock. From these results we draw our conclusions on the feasibility of our approach.

ERROR SCALING FOR HIGH-ALTITUDE GPS NAVIGATION

As a spacecraft travels away from Earth, the geometry it sees with respect to Earth-bound navigation sources progressively degrades, resulting in reduced achievable navigation accuracy. For two-way radiometric ranging systems, like DSN, lateral errors grow with increasing distance from Earth, but range errors remain stable, as local timing errors cancel. Conversely, in a one-way ranging system, such as GPS, where local timing errors do not cancel, it has been observed (e.g., [3, 12]) that range and clock errors grow more rapidly with distance than lateral errors, eventually becoming the dominant error source. In this section, we quantify this observation through a Dilution of Precision (DOP) analysis of a simplified high-altitude GPS problem. The analysis shows that, for GPS point positioning, lateral error standard-deviations grow linearly with distance from Earth, while range and clock error standard-deviations and their root-cross-covariances grow quadratically.

To gain some intuition, recall that range and clock bias are not independently measured, but are entwined in the pseudorange measurement. Far from Earth, identical range and clock increments will result in nearly identical changes to the pseudoranges. Lateral position errors, while becoming more sensitive to pseudorange error with increasing distance, are in some sense independent of clock error since lateral motion can be directly detected in the clock bias free difference of pseudoranges.

Consider the simple two-dimensional situation shown in Figure 1. Taking the usual approach to GPS point positioning and linearizing the pseudorange measurement equations, in this case around the point $(0, d, 0)$ in $(l, r, c) =$ (lateral, range, clock) coordinates, leads to

$$\underbrace{\begin{bmatrix} 1/z & d/z & 1 \\ 0 & 1 & 1 \\ -1/z & d/z & 1 \end{bmatrix}}_{H} \begin{bmatrix} \delta l \\ \delta r \\ \delta c \end{bmatrix} = \begin{bmatrix} \delta\rho_A \\ \delta\rho_B \\ \delta\rho_C \end{bmatrix} + n, \text{ with } \mathrm{Cov}(n) = \sigma^2 I, \tag{1}$$

where $z \equiv \sqrt{1+d^2}$, and each row of H is a unit vector from transmitter to receiver, augmented with a third column entry of 1 for clock bias, and n is zero mean white noise with component variance σ^2, as specified.

Letting H' be the transpose of the matrix H shown in Eq. (1), the covariance matrix of the least-squares state increments $(H'H)^{-1}H'\delta\rho$ is given by σ^2 times the so-called DOP matrix $(H'H)^{-1}$. It is instructive to numerically examine the form of this matrix for the case of $d \gg 1$. Doing so confirms the claimed decoupling of lateral errors from range/clock errors and the extreme correlation and large range/clock variances. One can

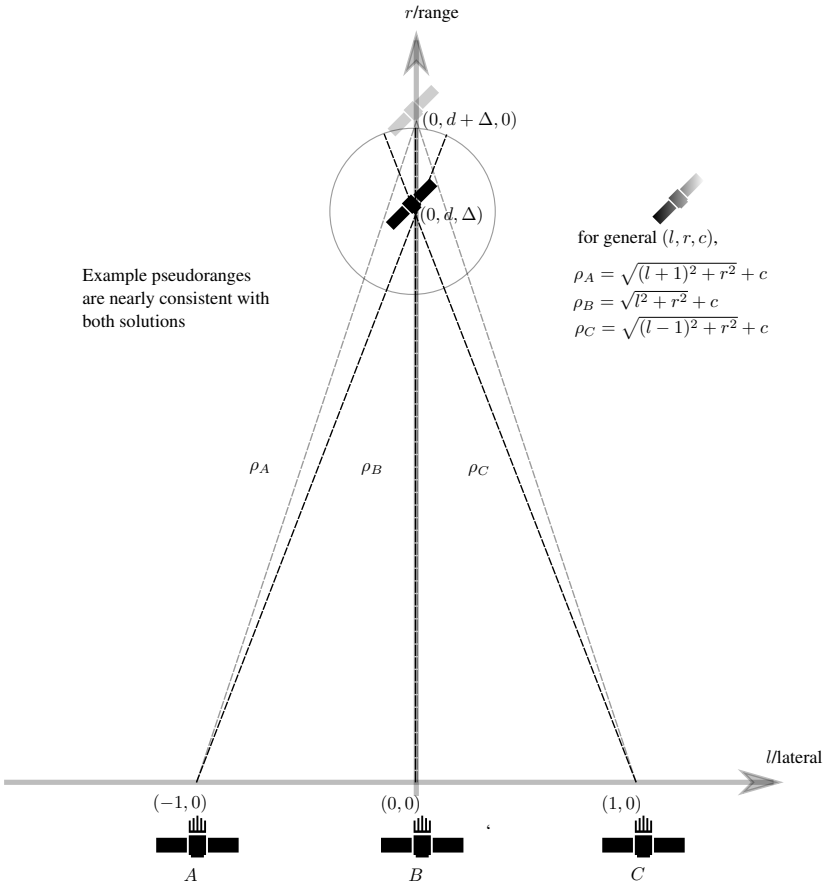

Figure 1: Simplified high-altitude GPS geometry.

also confirm that the square-root of the diagonal lateral component appears to scale in proportion with d while the range/clock component scale as d^2.

Next, we compute the DOP matrix in a series of steps to attempt to clarify the issues at hand. We start by replacing the pseudoranges from satellites A and C with half of their differences and sums, i.e., multiplying Eq. (1) by

$$U = \begin{bmatrix} 1/2 & 0 & -1/2 \\ 0 & 1 & 0 \\ 1/2 & 0 & 1/2 \end{bmatrix}.$$

This leads to

$$\begin{bmatrix} 1/z & 0 & 0 \\ 0 & 1 & 1 \\ 0 & d/z & 1 \end{bmatrix} \begin{bmatrix} \delta l \\ \delta r \\ \delta c \end{bmatrix} = \begin{bmatrix} \delta\rho^-_{AC} \\ \delta\rho_B \\ \delta\rho^+_{AC} \end{bmatrix} + n_2, \text{ with } \mathrm{Cov}(n_2) = \sigma^2 UU' = \sigma^2 \begin{bmatrix} 1/2 & 0 & 0 \\ 0 & 1 & 0 \\ 0 & 0 & 1/2 \end{bmatrix},$$

where $\delta\rho^-_{AC} \equiv \frac{1}{2}(\delta\rho_A - \delta\rho_C)$ and $\delta\rho^+_{AC} \equiv \frac{1}{2}(\delta\rho_A + \delta\rho_C)$. Immediately, we see that the lateral errors are decoupled and have the least-squares solution

$$\delta l = z\,\delta\rho^-_{AC} + n_l, \text{ with } \Sigma_l \equiv \mathrm{Cov}(n_l) = \frac{1}{2}\sigma^2 z^2 \approx \frac{1}{2}\sigma^2 d^2, \tag{2}$$

scaling as d^2. The range and clock errors now satisfy

$$\begin{bmatrix} 1 & 1 \\ d/z & 1 \end{bmatrix} \begin{bmatrix} \delta r \\ \delta c \end{bmatrix} = \begin{bmatrix} \delta\rho_B \\ \delta\rho^+_{AC} \end{bmatrix} + n_3, \text{ with } \mathrm{Cov}(n_3) = \sigma^2 D \text{ and } D \equiv \begin{bmatrix} 1 & 0 \\ 0 & 1/2 \end{bmatrix},$$

which are nearly linearly dependent equations as $d/z \approx 1$. Finally, multiplying through by

$$J = \begin{bmatrix} 1 & 1 \\ d/z & 1 \end{bmatrix}^{-1} = \frac{1}{1 - d/z} \begin{bmatrix} 1 & -1 \\ -d/z & 1 \end{bmatrix},$$

which compares the average of the outer pseudoranges to the middle pseudoranges, gives the least squares solution

$$\begin{bmatrix} \delta r \\ \delta c \end{bmatrix} = J \begin{bmatrix} \delta\rho_B \\ \delta\rho^+_{AC} \end{bmatrix} + n_{rc}, \text{ with } \Sigma rc := \mathrm{Cov}(n_{rc}),$$

with

$$\Sigma_{rc} \equiv \sigma^2 JDJ' = \frac{\sigma^2}{(1 - d/z)^2} \begin{bmatrix} 3/2 & -(1/2 + d/z) \\ -(1/2 + d/z) & 1/2 + (d/z)^2 \end{bmatrix}. \tag{3}$$

Recalling the definition of $z \equiv \sqrt{1 + d^2}$, gives

$$(1 - d/z) = 1 - \frac{1}{\sqrt{1 + \frac{1}{d^2}}} \approx \frac{1}{2d^2},$$

to first order in $1/d^2$. Substituting this approximation and $d/z \approx 1$ in Eq. (3), and recalling Eq. (2), gives

$$\Sigma_{rc} \approx \sigma^2 6d^4 \begin{bmatrix} 1 & -1 \\ -1 & 1 \end{bmatrix}, \text{ and } \Sigma_l \approx \sigma^2 \frac{d^2}{2},$$

for large d. Thus, indeed, for this high-altitude scenario, lateral error standard deviations scale as d while range and clock error standard deviations and their root-cross-covariances scale as d^2 for large $d \gg 1$.

A CONCEPT GPS NAVIGATION SYSTEM FOR GATEWAY

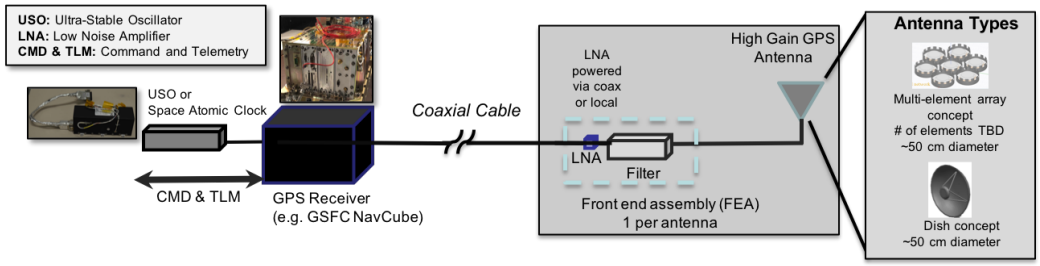

Figure 2: Concept Gateway GPS system.

Our concept GPS navigation system for Gateway is based on the MMS navigation system which, consists of the Navigator GPS receiver with a USO from Frequency Electronics, Inc. and the Goddard Enhanced Onboard Navigation System (GEONS) Extended Kalman Filter (EKF) flight software. The Navigator is a NASA Goddard Space Flight Center (GSFC) high-altitude C/A code GPS receiver with a powerful weak-signal acquisition engine that allows it to acquire and track sidelobe signals (< 25 dB-Hz) with no a-priori knowledge. Besides MMS, Navigator has flight heritage on the Space Shuttle Relative Navigation Sensor Experiment (2009) and the Global Precipitation Measurement Mission (GPM, 2014). Additionally, Navigator technology was incorporated into the Honeywell Orion GPS receiver to support fast-acquisition for rapid recovery after re-entry radio blackout (demonstrated December 2014). A next-generation version of Navigator, called the NavCube, has been delivered as part of the X-ray Communication (XCOM) experiment on the

International Space Station (ISS)-bound technology mission (STP-H6). GEONS development dates back to the 1980's for the Cosmic Origins Background Explorer, and it is currently flying on NASA's Terra, GPM, NICER/SEXTANT, and MMS missions. It is currently undergoing upgrades to support onboard navigation for the Restore-L mission. References [13] and [12] provide further detail on the MMS navigation system, including detailed flight results.

Reference [12] presents flight results from a MMS Phase 2B orbit with apogee at 25 RE and includes simulations of an MMS-like GPS navigation system in the lunar regime. In this paper we build on those results and propose a concept GPS system for Gateway based on the MMS navigation system with several modifications. First, as in [12], our concept GPS system would include an Earth-pointed high-gain GPS antenna with peak gain of 14 dB relative to an isotropic antenna (dBi). The roughly 7 dB increase over the peak MMS antenna gain would compensate for the Radio Frequency (RF) free space losses between MMS's current 25 RE apogee and the proposed lunar orbit. This target gain can be achieved with an approximately 50 cm diameter dish or multi-element array mounted on an Earth-pointed gimbal. The proposed antenna has a field of view of about 25° and will encompass the GPS constellation, which only subtends 8° at lunar distances. The combination of the Near-Rectilinear Halo Orbit (NRHO) and the Moon's orbit plane with respect to the ecliptic can result in the Gateway being 15° below the ecliptic plane at apolune. Accordingly, the antenna would ideally be collocated on a dedicated or shared Earth-pointed (e.g., communications antenna) 2-axis gimballed platform. However, by affixing the antenna with a small offset toward ecliptic north, a simple single-axis rotating platform could suffice to achieve the desired pointing accuracy. Second, we consider two reference oscillator options: a base option which makes use of an MMS-like USO, and a higher accuracy atomic clock modeled after the Spectratime Rubidium Atomic Frequency Standard (RAFS). The RAFS is a commercially-available product with a rich heritage that includes numerous units flying on Galileo GNSS satellites as well as other missions [10]. Figure 2 shows a diagram of our conceptual Gateway GPS system.

SIMULATION AND CALIBRATION

As in [12], the simulation results presented in this paper use the GEONS Ground MATLAB Simulation (GGMS), a MATLAB-based interface and analysis tool for running GEONS simulations. In this system, diagrammed in Figure 3, MATLAB routines are used as a simulation driver to setup GEONS data structures and call functions from a GEONS shared library. These functions are used to generate and process GPS and DSN measurements and perform state and covariance updates. The estimation data is then extracted by MATLAB for data analysis purposes.

This architecture provides considerable flexibility for the design of simulations while leveraging the heritage, verified mathematical models, and flight software from the GEONS library. The GGMS has the ability to operate from an external truth ephemerides or propagate a truth trajectory in real-time. Though not all utilized in this simulation, the system includes measurements models for numerous spacecraft sensors including GPS, ground station tracking, camera-based measurements (bearing to celestial body centers of mass, or surface landmarks), and laser range. Additionally the system can include maneuvers with random errors in the filter processing and perform Monte Carlo simulations.

GPS link calibration

Since publishing [12], we have made two significant improvements to the GEONS GPS simulation link model to enhance the fidelity of the GPS sidelobe signals. First, we replaced the two averaged GPS Block IIR and IIRM antenna patterns, which were based on ground measurements, with the recently published patterns for each GPS Space Vehicle (SV) that were constructed from flight data collected by the Antenna Characterization Experiment (ACE) project [6]. These patterns, which also include the Block IIF patterns, allowed us to simulate a much more complete and accurate constellation than in [12]. Figure 4a shows an example Block IIF pattern from the ACE dataset.* Second, and equally important to our goal of achieving

*The ACE patterns do not include GPS transmitter mainlobe data below 15° off-boresight angle. For the present simulations, we simply omitted these signals as they are rarely seen at high-altitude.

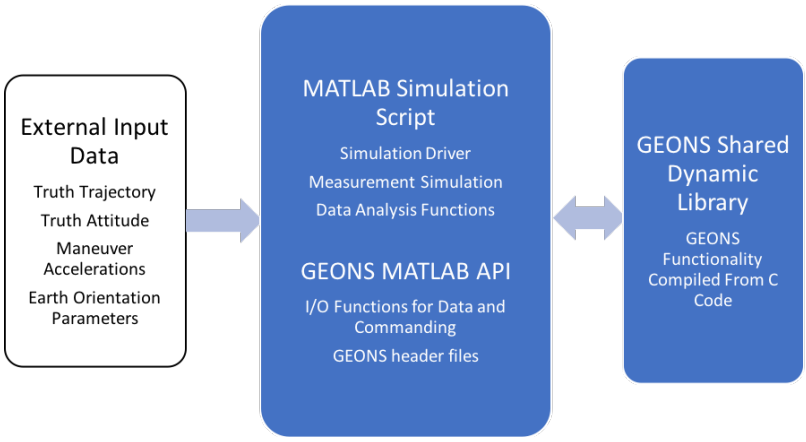

Figure 3: Overview of the GGMS and its relation to the GEONS package.

Parameter	Value
Antenna Temperature T_a	34 K
System Temperature T_{sys}	132 K
Implementation Loss R_{loss}	1.7 dB
Polarization Loss L_{pol}	1 dB
Block II/IIA $P_T(\max EIRP)$	17.9 dBW (31.6 dBW)
Block IIR $P_T(\max EIRP)$	17.3 dBW (29.2 dBW)
Block IIRM $P_T(\max EIRP)$	18.8 dBW (32.1 dBW)
Block IIF $P_T(\max EIRP)$	16.2 dBW (29.5 dBW)

Table 1: Link Parameters from analysis of MMS-Navigator GPS and high-altitude MMS flight data.

a consistent match between the on-orbit MMS GPS signal strengths and those that we were simulating, we incorporated the GPS yaw model from [1] into our simulation.

To calibrate the GPS-to-receiver link, we used the model equation

$$C/N_0 = P_T + G_T(\phi,\theta) - 20\log(4\pi/\lambda_{L1}) + G_R(\phi,\theta) - L_{pol} - 10\log(k\,T_{sys}) - R_{loss}, \qquad (4)$$

where λ_{L1} is the GPS L1 carrier wavelength, k is the Boltzmann constant, and the remaining parameter definitions and values are summarized in Table 1. To establish the receiver system noise temperature $T_{sys} = T_a + T_r$ for the MMS Navigator GPS receiver, we estimated the antenna temperature $T_a = 34\ K$ at high altitude by integrating the MMS receiver antenna pattern over a piecewise constant space temperature profile with the following assumptions: the disc of the Earth at 290 K as viewed from 25 Re, a deep space background of 4 K, and a spacecraft worst-case specified temperature of 313 K in the antenna back-lobe. The receiver noise temperature T_r is the result of a cascade of the following components: an estimated 0.25 dB antenna resistive and cable losses (assumed at a physical temperature of 313 K), an integrated front end electronics assembly noise figure of 1.0 dB (referenced to 290 K), and a baseband processing loss R_{loss} measured at 1.7 dB. This last term is mainly the result of pre-correlation filtering and non-ideal analog-to-digital conversion. We also assumed a polarization loss L_{pol} between transmit and receive antenna of 1 dB.

The transmitter antenna gain patterns G_T were provided as a function of off-boresight angle (elevation) θ and azimuth ϕ in the ACE datasets. For the receiver gain pattern G_R, we used a model of the composite MMS receive pattern that provides peak gain of approximately 6.3 dBi in the ecliptic plane. A more thorough description on the MMS antenna configuration can be found in [13].

Finally, we adjusted the transmit power P_T on a per-GPS-block basis to match an eight-day period of MMS Observatory-1's flight data from early in the mission's Phase 2B orbit. Starting from the beginning of

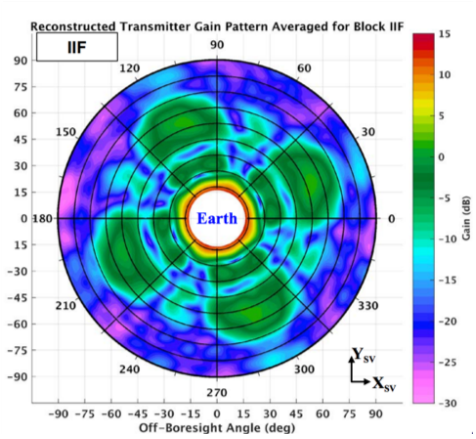

(a) Example GPS ACE recovered block IIF transmit pattern [6], used in the simulation link calibration.

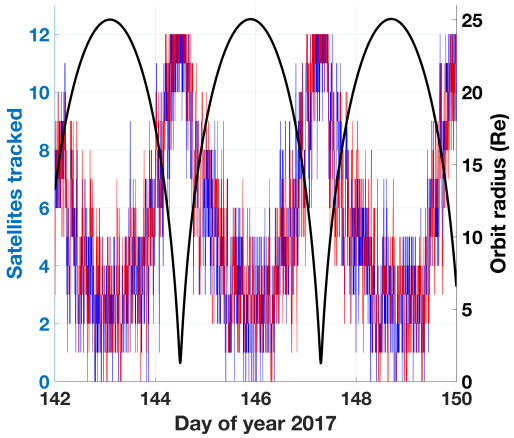

(b) Simulated (red) vs. flight (blue) number of GPS signals tracked for the MMS Phase 2B calibration.

Figure 4: Aspects of the GGMS simulation GPS calibration.

this data window, we ran the GGMS simulation and compared predicted C/N_0 levels to MMS flight C/N_0 levels over periods when the observatory was at a radial distance above 10 RE. The P_T levels for each of the three main GPS blocks (IIR, IIR-M, and IIF) were then adjusted to minimize the C/N_0 difference. Since the purpose of our calibration is to accurately model signals at very high altitudes, we only considered data in regions when the MMS spacecraft was above 10 RE. For lower altitudes, a more complicated model of antenna noise and multi-access interference power is required.

Using this calibrated model, we obtained a good qualitative match to the number of signals tracked, as shown in Figure 4b. We note that an exact match is not expected since the acquisition process is inherently random in the simulation. Additionally, we obtained a good match to the C/N_0 tracking arcs as shown in Figure 5. Unlike in [12], where we had settled for qualitatively similar behavior in sidelobe C/N_0 tracking arcs, the C/N_0 values in the updated simulation are accurate to within 1-2 dB (1σ). These results make us confident that when the GGMS simulation is re-targeted to the Gateway orbit, the signal environment will be accurately modeled.

The transmit power values obtained, along with the link parameters used in the model, Eq. (4), are summarized in Table 1 for reference. However, we do not suggest these values be taken as definitive absolute estimates of GPS transmit power, apart from our simulation, as there is uncertainty in the T_a, T_r and L_{pol} assumptions, and possibly in the absolute gain levels in the ACE patterns, that could lead to uncertainty in the transmit power estimates.

Receiver clock models

In the navigation performance simulations presented below, we used the MMS Phase 2B calibrated GPS simulation model described above and considered two oscillator models: an MMS USO and a more stable commercial atomic clock, namely the Spectratime RAFS [10]. To model these clocks in the simulation, we used a thrice-integrated white noise process with the intensities (variance per unit time) of the driving white noises specified by three parameters q_1, q_2, q_3, for bias, rate, and acceleration noise intensities, respectively. This same integrated noise model is used for the GPS clocks in the GPS Master Control Segment (MCS), as described in [8], where the authors show that the Hadamard variance $\sigma_H^2(\tau)$ at interval τ, produced by this model is given by

$$\sigma_H^2(\tau) = q_1\,\tau^{-1} + \frac{1}{6}\,q_2\,\tau + \frac{11}{120}\,q_3\,\tau^3. \tag{5}$$

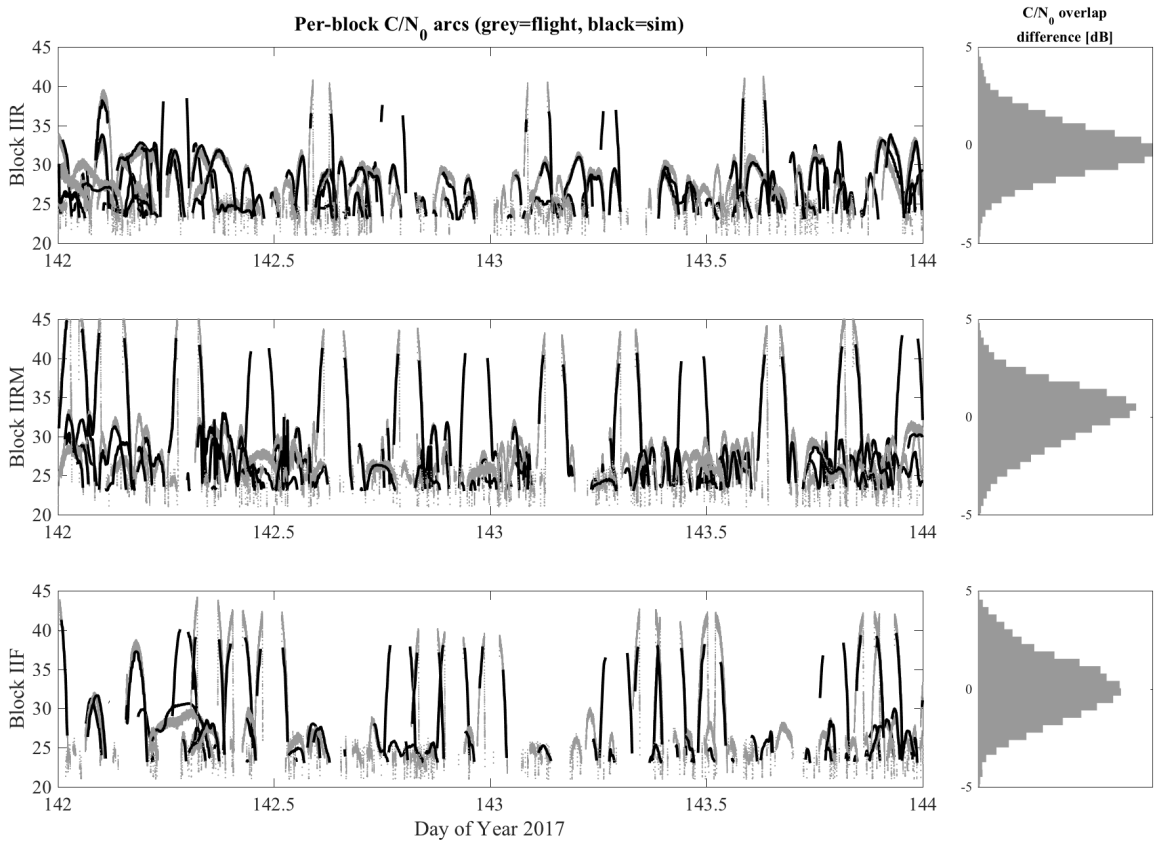

Figure 5: MMS flight signal C/N_0 (gray) versus GEONS GPS simulation, using ACE patterns and GPS yaw model, simulated tracked C/N_0 (black), separated per major GPS block, along with overlap difference histograms. Sidelobe signals can be easily distinguished as those arcs that remain under 30 dB-Hz. The mainlobe signals rise up to 40 dB-Hz or higher and then disappear as they are occulted by the Earth, re-emerging on the other side. (The difference in the mainlobe near Earth occultation is due to an atmosphere mask of 1,000 km in the simulation, not present in the tracking data, although the onboard filter rejects any measurement below 1,000 km altitude.)

Using Eq. (5), we fit the *q-parameter* model to Hadamard variance data from the MMS USO specification and the RAFS typical performance data presented in [10]. Figure 6 shows the resulting Hadamard variance plots of specification and fit models. Table 2 lists the fit q-parameters.

Lunar Gateway NRHO simulation trajectory

The target orbit currently proposed for the Gateway is an Earth-Moon L2 Southern NRHO with an average perilune altitude of approximately 1,800 km, an apolune altitude of 68,000 km, and a period of roughly 6.5 days. This orbit exhibits a 9:2 resonance with the Moon's orbit. Figure 7 shows the NRHO as viewed in the rotating system from the Earth-Moon line, which lies below the plane of the Moon's orbit. The truth trajectories used in this study were generated using the high-precision orbit propagator in the FreeFlyer Astrodynamic Software. Details on the generation of the truth trajectories are provided in [11], including the orbit maintenance maneuvers that are executed at each apolune to maintain the quasi-periodic orbit.

The Gateway is expected to support crewed operation as well as longer uncrewed periods. When crewed, trajectory perturbation sources ranging from waste water dumps or attitude correction perturbations are expected. These perturbations could be due to increased angular momentum from high intensity operations or even crew exercise. The sum of the resulting perturbations will increase the cadence of orbit maintenance

Parameter	Value (USO)	Value (RAFS)
$q_1\ [s^2/s]$	1.20×10^{-22}	3.70×10^{-24}
$q_2\ [s^2/s^3]$	1.58×10^{-26}	1.87×10^{-33}
$q_3\ [s^2/s^5]$	1.00×10^{-38}	7.56×10^{-59}

Table 2: Linear model oscillator q-parameters for USO and RAFS.

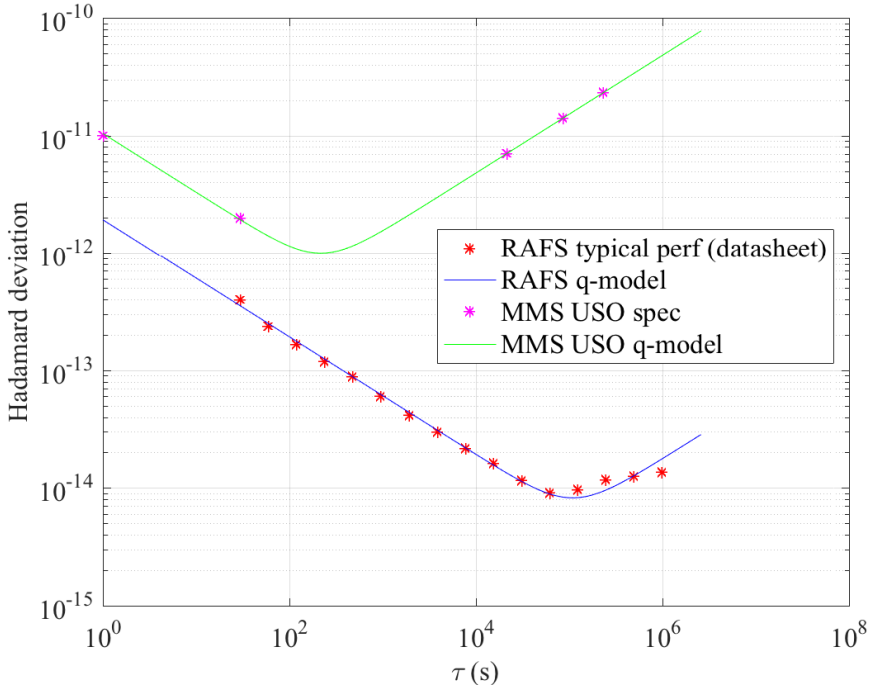

Figure 6: Specification/typical performance Hadamard variance for the MMS USO and Spectratime RAFS used in the GPS simulations (stars) along with simulation/estimation model (solid lines).

maneuvers and operations for momentum unloads. In contrast, uncrewed operations are expected to be relatively benign, with perturbations limited to physical mismodeling of the space environment or maneuver execution errors.

Following [11], we separately examine the NRHO under quiescent uncrewed and noisier crewed disturbance scenarios. The orbit maintenance maneuvers are modeled in the filter with errors of 3% (1σ) of the planned ΔVs. Table 3 lists the dynamic models used in the truth trajectory and the GEONS onboard filter. Again following [11], the area and mass were chosen to approximate the Orion spacecraft. In addition, for the crewed scenario, the disturbances listed in Table 3 are modeled by periodically incorporating random ΔV vectors to the filter dynamics without incorporating them into the truth trajectory.*

Before running our navigation simulations, GEONS propagation of the uncrewed NRHO trajectory was validated through comparison with a FreeFlyer trajectory that used nearly identical dynamic models. Agreement to within 10 m and 2 mm/s at perilune was achieved after a 1-orbit propagation. For the models listed in Table 4, the propagation differences increase to about 200 m and 4.5 cm/s at perilune after a 1-orbit propagation. The process noise used to model the errors in the propagation was calibrated to be consistent with these observations. For the uncrewed trajectory, the process noise model was scaled based on the distance from the Moon because lunar gravity was the dominant force acting on the spacecraft. For the crewed trajectory, an

*An alternative approach to modelling crew activity is to use an *episodic* process noise model based on compound-Poisson/Gaussian process as described in [4, Chapter 2].

*PSA stands for Pressure Swing Adsorption. This is part of the CO_2 removal system.

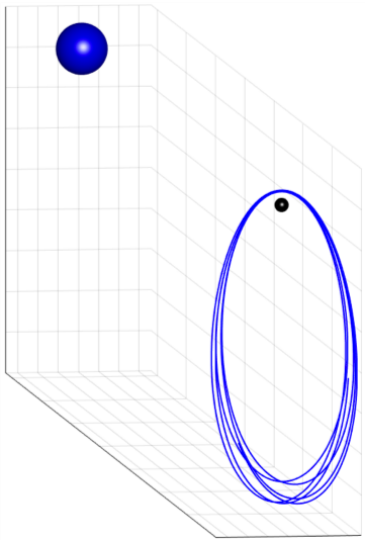

Figure 7: Earth-Moon L2 Southern NRHO in rotating coordinates proposed for the Lunar Gateway.

Disturbance	ΔV Magnitude	Period
PSA puffs*	8.3480×10^{-4} m/s	10 min
Attitude deadbands	2.0043×10^{-5} m/s	70 min
Attitude slews	6.9751×10^{-4} m/s	3.2 hours
Wastewater dumps	1.8840×10^{-3} m/s	3.0 hours

Table 3: Disturbances modeled in *Crewed* trajectory from [11].

additional constant process noise contribution was included to model the additional disturbances.

Ground station tracking baseline configuration and validation

Reference [11] provides results from Monte Carlo simulations performed to characterize the navigation accuracy achievable for both the NRHO uncrewed and crewed trajectories using DSN-like two-way range and Doppler measurements for several different tracking schedules. To provide a means of comparison of navigation achievable using GPS measurement versus GS tracking measurements for the current study, GS measurements were simulated and processed using the GGMS and GEONS. For both the GS and the GPS simulations, a 40-case Monte Carlo simulation was run that varied initial state errors, measurement noises

	Truth Trajectory Simulation	GEONS Filter Propagation
Planetary Ephemeris	JPL DE 430	JPL DE421
Pont Mass Gravity	Sun, Earth, Venus, Mars, Jupiter, Saturn	Sun, Earth, Venus, Mars, Jupiter, Saturn
Lunar Gravity Model	30x30 GRAIL PRIM660	30x30 LP100K
Solar Radiation Pressure	Spherical 24,000 kg, $80\,\mathrm{m}^2$, CR $= 2.0$	Spherical 24,000 kg, $80\,\mathrm{m}^2$, CR $= 2.0 + 0.2\,(1\sigma)$
Orbit Maintenance	ΔVs at apoapsis Planned	Planned + $3\%\,(1\sigma)$ Maneuver execution error

Table 4: Dynamic models used in simulation.

Noise/Bias Type	Value (1σ)
Measurement Rate	30 s
Range Noise	4.0 m
Range Bias	0.5 m
Doppler Noise	0.5 cm/s
Doppler Averaging Interval	30 s

Table 5: Ground tracking simulation parameters.

and biases, maneuver disturbances, and solar radiation pressure coefficient errors.* In the ground tracking scenario, only Gateway position and velocity states were estimated. The initial covariance assumed the a priori states were anchored by sufficient ground tracking (and/or GPS) and is reflective of uncertainties equivalent to 1 km (1σ) and 0.02 m/s (1σ) each axis. For the ground tracking baseline, we used a tracking schedule of eight hours of two-way range and Doppler tracking from a single station each day alternating between stations located at Canberra (Australia), Goldstone (California), and Madrid (Spain). Table 5 lists the ground tracking measurement assumptions used in this study which are modeled on, though not identical to, a medium-level-of-tracking case used in [11]. It is worth noting that the level of tracking used here is roughly twice as dense as the 3 passes/week plan used in [9].

Our GGMS GS simulation results were validated by comparing to the results provided in [11] for the same tracking schedule. In both the uncrewed and crewed cases, we obtained fully consistent results.

GPS configurations

For the next set of simulations we configured the GGMS to model the Navigator GPS in the Gateway NRHO under the crewed and uncrewed disturbance scenarios. We used the calibrated GPS model parameters described above, but included the 14 dBi high-gain antenna,† and either the MMS-like USO or the RAFS clock models.

For the GPS cases, in addition to position and velocity states, we estimate clock bias, rate, and acceleration. The initial position and velocity covariances were set to the same values as the GS configuration given in the previous section, and the initial clock root-covariance and errors were set to $0.5\,\text{s}$, 2×10^{-7} s/s, 1.2×10^{-15} s/s^2. Up to 12 GPS pseudorange measurements were simulated every 30 s with a simple additive random error model of 10 m below, and 4 m above, a 40 dB-Hz *strong signal* threshold (all 1σ). GPS visibility was assessed based on the GPS link model, Eq. (4), a receiver sensitivity of 23 dB-Hz, and a probabilistic model of the Navigator receiver's acquisition and tracking performance.

Figure 8 shows the number of GPS signals tracked and C/N_0 for a typical GPS run where the receiver tracked 3 GPS signals on average, with a standard deviation of about 1.5 signals. Complete outages were rare and brief. Most tracked signals are weak sidelobe transmissions below 30 dB-Hz. This is consistent with our expectation that the visibility at lunar distance with the concept 14 dBi high-gain antenna should be similar to that seen on-orbit at MMS Phase 2B apogee. Tracking performance looks similar at all points in the simulation since the view to the GPS constellation is similar throughout the NRHO.

*The Monte Carlo simulations were limited to 40 cases to meet constraints in preparing the paper. While this is a modest size, we argue here that it provides reasonable confidence in the results. Assuming the filter errors at each point-in-time across trials are independent and identically-distributed Gaussians, (an assumption that holds only approximately at best), then e.g., a 90% confidence interval for the population standard deviations σ may be obtained as $\{\sqrt{(M-1)}s/\sqrt{b} \leq \sigma \leq \sqrt{(M-1)}s/\sqrt{a})\}$, where s is the sample standard deviation, $M = 40$ and a and b are 0.05 and 0.95 critical values of a χ^2-distribution with $M-1$ degrees of freedom, c.f., [5]. The length of this interval relative to s is a reasonably small, constant 39%. With a bit more effort, a confidence interval for the population Root Mean Square (RMS) error, whose orbit averages are used for summary statistics below, can be obtained whose length relative to the sample RMS has been observed to be limited to around 60%.

†To model the high-gain antenna, we used the MMS antenna pattern and orientation and simply changed its peak gain value to 14 dBi. Thus, like MMS, the antenna is doughnut-shaped with peak gain remaining approximately in the ecliptic plane. This does not correctly model the concept antenna, a deficiency we intend to update in future work. For the purposes of this analysis, it is conservative assuming a two-axis antenna pointing platform, since the concept system's antenna boresight would remain pointed at the Earth to within a few degrees, whereas in the present simulation, GPS signals can be received off-boresight up to 15° near apolune.

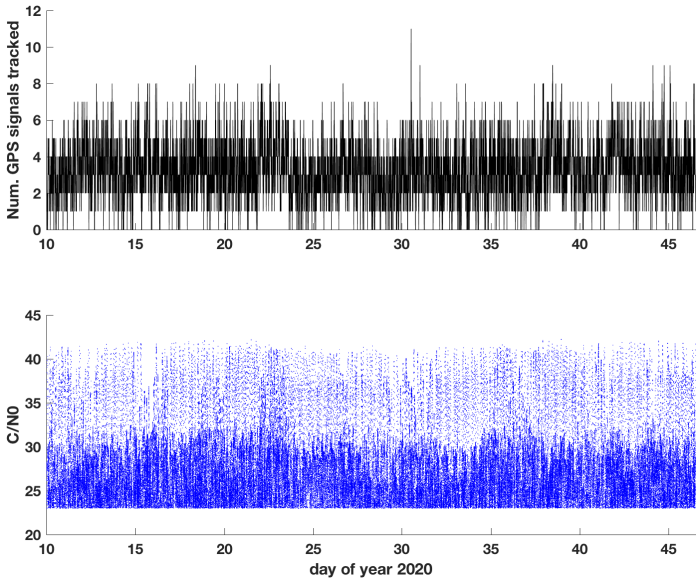

Figure 8: Typical number of GPS signals tracked (top) and C/N_0 (bottom) in the NRHO.

SIMULATION RESULTS FOR THE UNCREWED TRAJECTORY

Figure 9 shows navigation results on the uncrewed trajectory from the 40-case Monte Carlo simulation for each of the three sensor configurations. The top row of plots show the GS baseline, the middle row has GPS with the USO, and the bottom row shows GPS with the RAFS. Position errors are shown on the left and velocity errors are shown on the right. Each position or velocity result is presented as a pair of subplots with the range error (along the direction from the center of the Earth to the Gateway) shown on the top, and Root Sum Square (RSS) lateral error (in the plane perpendicular to the range direction) shown on the bottom. Clock errors are not shown for the GPS configurations since they are essentially the same as the range errors due to the high correlation between range and clock errors at lunar distances. Recall that clock errors are not estimated for the GS configurations. In each plot, the individual error trajectories are shown in thin grey lines, while the mean over the 40 cases of the 3-sigma root-covariance is shown in a thick green line. Table 6 provides summary statistics for each configuration split into range and RSS lateral error components computed as 3-times the RMS error taken over the 40 Monte Carlo runs. This is similar to a 3-sigma error but without the mean removed. This metric is then averaged over the last 6.5 day orbit of the simulation.*

We note the following observations:

- GPS lateral position and velocity errors are very similar for the two GPS clock configurations and are far smaller than the GS baseline.
- The GS baseline has superior range position and velocity performance compared to the GPS with USO configuration, reflecting the challenge of resolving range and clock errors.
- After an initial convergence period, the range and range velocity errors for the GPS with RAFS configuration become much smaller than the GS baseline, so that the GPS with RAFS performance completely outperforms that of the GS baseline after a few orbits. This convergence time will be reduced if we were to start with a smaller initial clock error, recalling that we initialized the filter with a relatively large $0.5\,\mathrm{s}$ (1σ) clock bias error.

*It may be more valuable to compute such summary statistics averaged over time intervals just prior to the apolune orbit maintenance maneuvers, rather than averaged over the final orbit, since current Gateway requirements seem to focus on velocity knowledge available for planning these maneuvers, see [9]. Such errors can be estimated from our results by examining the plots just prior to the apolune maneuver, which is apparent from the minor velocity spike that occurs after each maneuver, halfway between pairs of larger perilune spikes.

Uncrewed scenario - 3-RMS error, averaged over last orbit				
	Pos Range	Pos RSS Lateral	Vel Range	Vel RSS Lateral
Ground Tracking	32.9 m	467.4 m	1.0 mm/s	10.6 mm/s
GPS with USO	202.9 m	31.3 m	1.9 mm/s	1.4 mm/s
GPS with RAFS	8.5 m	30.5 m	0.2 mm/s	1.2 mm/s

Table 6: Uncrewed scenario summary statistics.

Crewed scenario - 3-RMS error, averaged over last orbit				
	Pos Range	Pos RSS Lateral	Vel Range	Vel RSS Lateral
Ground Tracking	450.5 m	8143.8 m	18.3 mm/s	155.3 mm/s
GPS with USO	909.7 m	79.0 m	18.9 mm/s	12.3 mm/s
GPS with RAFS	21.4 m	76.9 m	3.5 mm/s	11.9 mm/s

Table 7: Crewed scenario summary statistics.

- The velocity errors show a major spike at each perilune, and a minor spike at the apolune orbit maintenance maneuver. The perilune spike is in-part due to the additional process noise added there to prevent divergence, and in-part inherent in the weak stability of the NRHO. The minor spike after the maneuver may be reduced through the use of a high-quality Inertial Measurement Unit (IMU) to sense accelerations more accurately than the modeled 3% (1σ) maneuver error.
- The perilune velocity error spike generally integrates up to a position error spike except, perhaps interestingly, in the GPS configurations for the range component of position. Instead, the GPS range errors seem to be minimized at perilune. A possible explanation for this observation is that high perilune dynamics and additional process noise added thereabouts reduces the range and clock correlation and allows the filter to resolve the range component of error much better. By plotting the range and clock error correlation coefficient, not included here, we observed that it does indeed reduce abruptly at each perilune pass.

SIMULATION RESULTS FOR THE CREWED TRAJECTORY

Figure 10 and Table 7 show analogous results for the crewed scenario. A similar set of observations can be made here as for the uncrewed scenario. However, in the crewed scenario, the benefits of GPS over the GS baseline appear to be amplified. In all configurations, the additional disturbances from the crew operations result in degraded performance relative to the uncrewed scenario, but the degradation seems to be significantly worse for the baseline GS configuration. For example, while the GPS lateral position summary errors, again similar for two GPS configurations, approximately double as compared to the uncrewed scenario, the baseline GS lateral errors increase by a factor of almost 20. While the position range error summary statistics for the GS configuration are still better than the GPS with USO, the difference is smaller compared to the uncrewed case, and the range velocity errors are almost the same for GPS with USO when compared with the GS baseline. Finally, we note that the GPS with RAFS, after convergence, again outperforms the GS baseline, but by a significantly larger factor than in the uncrewed scenario.

CONCLUSION

The simulations presented in this paper make use of two recent high-altitude GPS datasets, the flight results from the Magnetospheric Multiscale Mission and the measured GPS transmit patterns from the GPS Antenna Characterization Experiment, to provide a well-calibrated prediction of the performance of a GPS based navigation system for the proposed Lunar Gateway. The concept system is based on the MMS GPS navigation system, currently navigating the four MMS spacecraft in elliptic orbits with apogee at 40% lunar distance, augmented with a roughly 50 cm high-gain antenna and, optionally, with an atomic clock. The results are clear: GPS can provide a simple, high-performance, onboard, autonomous navigation solution for

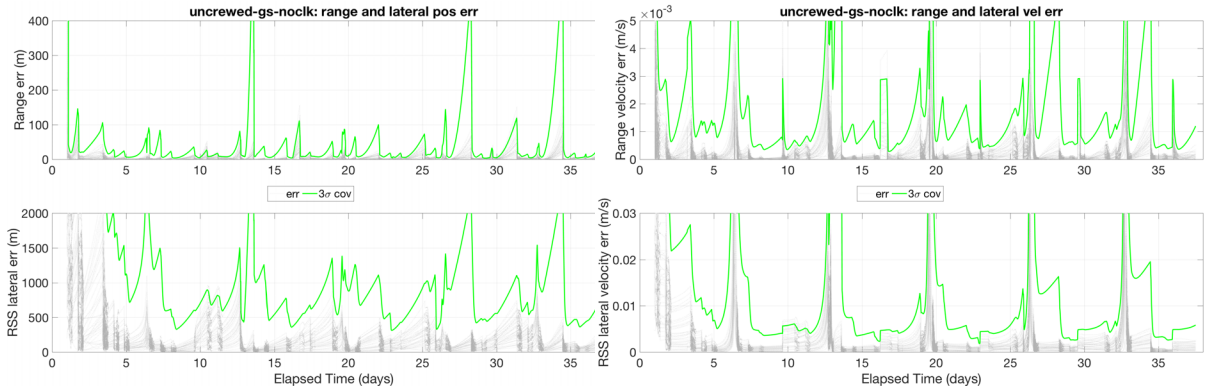

(a) Ground tracking position.

(b) Ground tracking velocity.

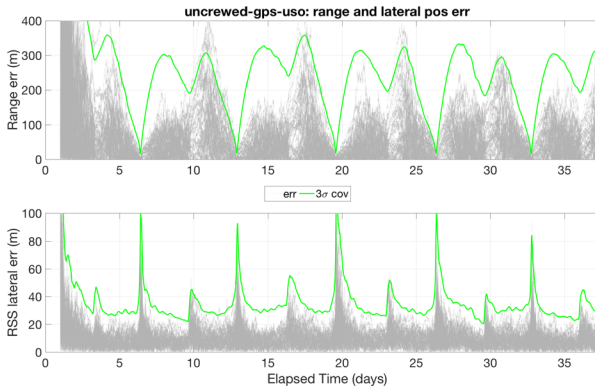

(c) GPS with USO position.

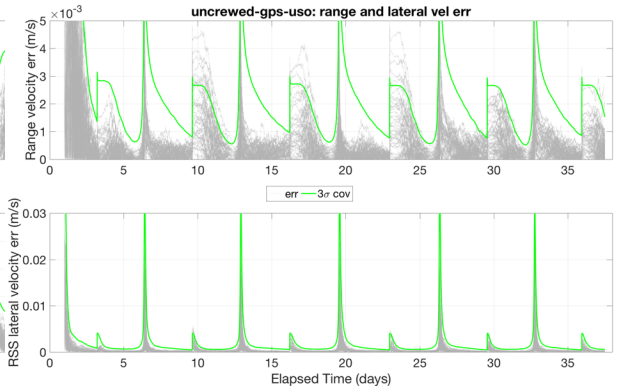

(d) GPS with USO velocity.

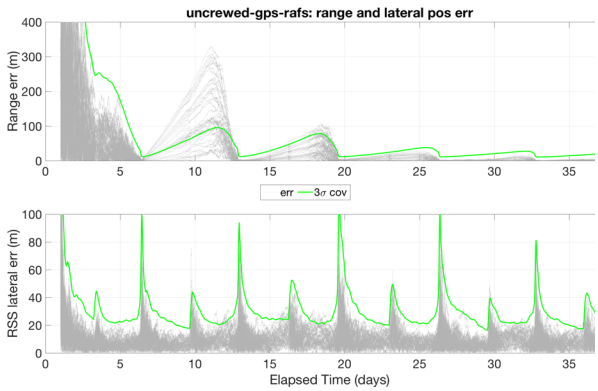

(e) GPS with RAFS position.

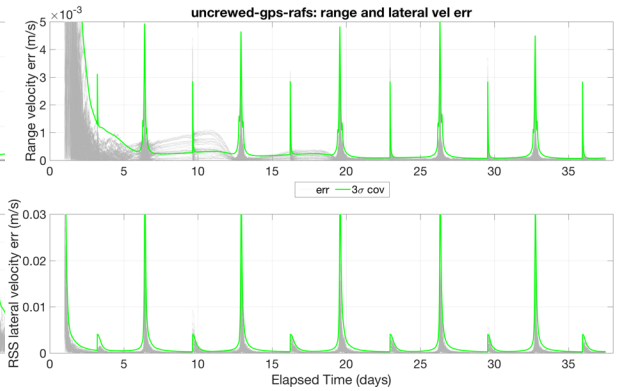

(f) GPS with RAFS velocity.

Figure 9: Navigation performance on the *uncrewed* trajectory. Ground tracking baseline (top), GPS with USO (middle), and GPS with RAFS (bottom).

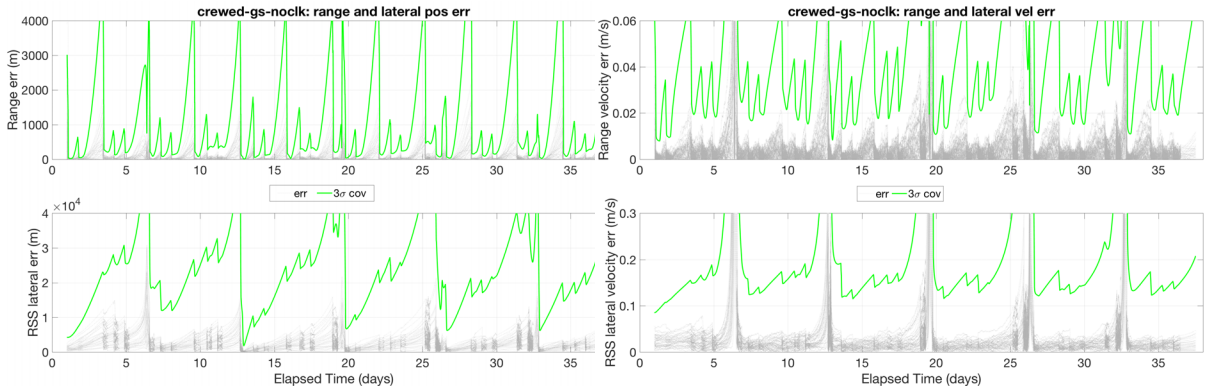

(a) Ground tracking position.

(b) Ground tracking velocity.

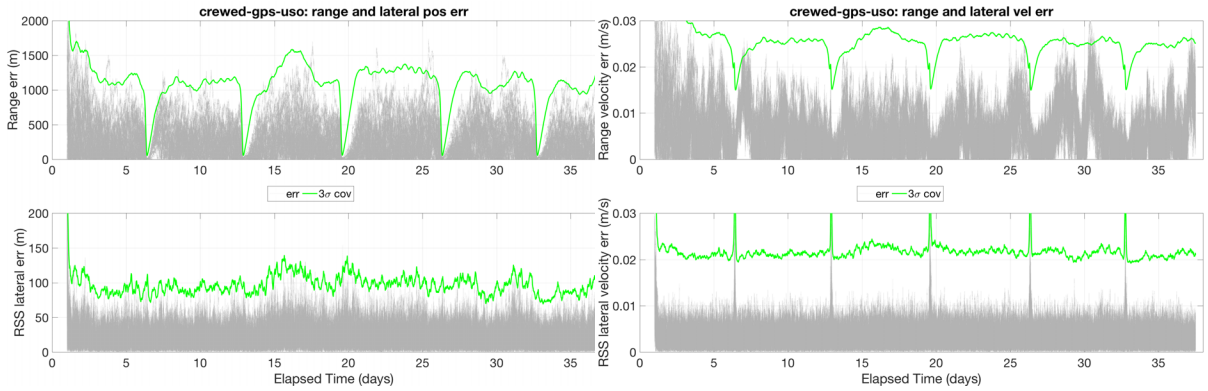

(c) GPS with USO position.

(d) GPS with USO velocity.

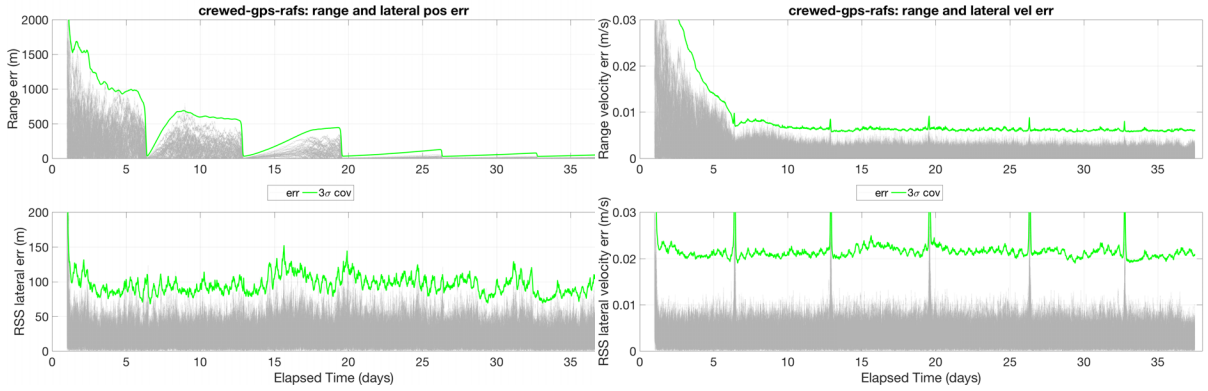

(e) GPS with RAFS position.

(f) GPS with RAFS velocity.

Figure 10: Navigation performance on the *crewed* trajectory. Ground tracking baseline (top), GPS with USO (middle), and GPS with RAFS (bottom).

the Lunar Gateway and likely for other missions in the lunar regime. As compared to a specific conceptual ground-tracking baseline simulation also presented in this paper, the GPS solution offers improved performance for many or all metrics (depending on the clock modeled), an accurate local clock solution, continuous real-time and onboard solution availability, and reduced ground-tracking and operations costs. Alternatively, GPS/GNSS could be combined with ground-tracking and/or other sensors as part of a complementary navigation suite providing enhanced performance and robustness.

FUTURE WORK

Future work includes running extended and enhanced simulations, including hardware-in-the-loop tests, as well as investigating multi-frequency and multi-GNSS, precision carrier phase observables, and enhanced weak-signal signal processing techniques. Other areas include the benefits of GPS for rendezvous and other relative navigation scenarios, and assessing the impact of and mitigations for GPS/GNSS interference.

ACKNOWLEDGMENT

The authors wish to thank Mitra Farahmand, Russell Carpenter, and Jason Mitchell for helpful discussions and feedback on the paper, and to Michael Volle for providing extensive support with the NRHO trajectory.

REFERENCES

[1] Yoaz E. Bar-Sever. A New Model for Yaw Attitude of Global Positioning System Satellites. Report TDA Progress Report 42-123, Jet Propulsion Laboratory, 1995.

[2] Frank H. Bauer, Joel J. K. Parker, Bryan Welch, and Werner Enderle. Developing a Robust, Interoperable GNSS Space Service Volume for the Global Space User Community. In *Proceedings of the Institute of Navigation International Technical Meeting*, January 2017.

[3] J. Russell Carpenter, David C. Folta, Michael C. Moreau, and David A. Quinn. Libration Point Navigation Concepts Supporting the Vision for Space Exploration. In *AIAA/AAS Astrodynamics Specialist Conference*. AIAA, 2004.

[4] Russell Carpenter and Chris D'Souza. Navigation Filter Best Practices. Technical Report TP-2018-219822, NASA, April 2018.

[5] George Casella and Roger L. Berger. *Statistical Inference, 2nd ed.* Duxbury, 2002.

[6] Jennifer E. Donaldson, Joel J. K. Parker, Michael C. Moreau, Dolan E. Highsmith, and Phillip Martzen. Characterization of On-Orbit GPS Transmit Antenna Patterns for Space Users. In *Proceedings of the Institute of Navigation GNSS+*, September 2018.

[7] Cheryl Warner (editor). NASA's Lunar Outpost will Extend Human Presence in Deep Space. *https://www.nasa.gov/feature/nasa-s-lunar-outpost-will-extend-human-presence-in-deep-space*, May 2018.

[8] Steven T. Hutsell, Wilson G. Reid, Lt Jeffrey D. Crum, Lt H. Shawn Mobbs, and James A. Buisson. Operational Use of the Hadamard Variance in GPS. In *Proceedings of the 28th Annual Precise Time and Time Interval Systems and Applications Meeting/Proceedings of the Institute of Navigation GNSS+*, pages 201–214, December.

[9] Clark P. Newman, Diane C. Davis, Ryan J. Whitley, Joseph R. Guinn, , and Mark S. Ryne. Stationkeeping, Orbit Determination, and Attitude Control for Spacecraft in Near Rectilinear Halo Orbits. In *Proceedings of the AAS/AIAA Astrodynamics Specialist Conference*, number 18-388. Univelt, 2018.

[10] Spectratime. iSpace+^{TM} Space-Qualified Rubidium Atomic Frequency Standard Specification, Revision 3.0. *https://www.spectratime.com/uploads/documents/ispace/iSpace_RAFS_Spec.pdf*, November 2016.

[11] Michael Volle and Dianne Davis. Examining the Feasibility of Relative-Only Navigation for Crewed Missions to Near Rectilinear Halo Orbits. In *Proceedings of the AAS/AIAA Astrodynamics Specialist Conference*, number 18-351. Univelt, 2018.

[12] Luke B. Winternitz, William A. Bamford, and Samuel R. Price. New High-Altitude GPS Navigation Results from the Magnetospheric Multiscale Spacecraft and Simulations at Lunar Distances. In *Proceedings of the Institute of Navigation GNSS+*, September 2017.

[13] Luke B. Winternitz, William A. Bamford, Samuel R. Price, J. Russell Carpenter, Anne C. Long, and Mitra Farahmand. Global Positioning System Navigation Above 76,000 KM for NASA'S Magnetospheric Multiscale Mission. *NAVIGATION, Journal of The Institute of Navigation*, 64(2):289–300, August 2017.